

Si-doped ZnAl-LDH nanosheets by layer-engineering for efficient photoelectrocatalytic water splitting

Wentao Bao^{a,1}, Ying Tang^{a,1}, Jie Yu^a, Wenxia Yan^a, Chenxu Wang^a, Yangyang Li^a, Zhimou Wang^a, Jinfeng Yang^{a,*}, Lili Zhang^{b,*}, Feng Yu^{a,c,**}

^a Key Laboratory for Green Processing of Chemical Engineering of Xinjiang Bingtuan, School of Chemistry and Chemical Engineering, Shihezi University, Shihezi 832003, China

^b Institute of Sustainability for Chemicals, Energy and Environment (ISCE2), Agency for Science, Technology and Research (A*STAR), Jurong Island 627833, Singapore

^c Carbon Neutralization and Environmental Catalytic Technology Laboratory (CN&ECT Lab), Bingtuan Industrial Technology Research Institute, Shihezi University, Shihezi 832003, China

ARTICLE INFO

Keywords:

Amorphous nanosheets
Exfoliation
Layered double hydroxide
Electron-hole pairs
Water splitting

ABSTRACT

A highly efficient Si-doped ZnAl-LDH (denoted as Si-ZnAl-LDH nanosheet) catalyst that is derived from large-area chemical exfoliation for photoelectrocatalytic water splitting. The formation of amorphous Si-ZnAl-LDH nanosheets through chemical exfoliation or layer engineering leads to much more accessible surfaces that originally are not accessible in highly crystalline ZnAl-LDH sheets. The incorporation of Si to highly exfoliated ZnAl-LDH nanosheets generates more oxygen vacancies, increases the number of active sites, redistributes the local charge density of the active centers and effectively suppresses the recombination of the generated electron-hole pairs. Specifically, the overpotential of HER and OER for Si-ZnAl-LDH nanosheet is 108 mV and 260 mV, respectively, at current density of 10 mA cm⁻² under light-assisted conditions. Total applied voltage is 1.673 V for water splitting in a full cell. This work provides a novel chemical exfoliation or layer-engineering strategy for the synthesis of scalable and cost-effective LDH nanosheets with efficient photoelectric response.

1. Introduction

Energy and environmental problems have gained increasing attention and there is a strong push to look for alternative sustainable and clean solutions [1,2]. Hydrogen is considered as one of the alternative clean energy sources because of its high energy density and environmental friendliness [3,4]. Photo-assisted electrocatalytic or photoelectrocatalytic water splitting which involves hydrogen evolution reaction (HER) [5] at the cathode and oxygen evolution reaction (OER) at the cathode with light and renewable electricity is a promising route to harvest sustainable and eco-friendly H₂ for chemicals and energy sectors [6,7]. The key to achieving high utilization of light energy lies in the design and fabrication of semiconductor photoelectrodes that improve visible light absorption, photoexcited carrier separation/-transfer efficiency, and oxygen precipitation reaction kinetics [8]. In recent years, two-dimensional (2D) layered materials have been

increasingly favored due to their unique optoelectronic catalytic properties [9].

2D LDH have attracted great attention as promising catalysts for water splitting with their highly flexible and tunable chemical composition and physical properties [10]. To date, various physical and chemical strategies have been explored to improve the catalytic properties of LDH [11]. The efforts include introducing defects and vacancies on LDH by chemical etching, plasma or laser techniques [12,13], forming monoatomic complexes and/or metal organic backbone complexes [14,15], modulating LDH by means of interlayer anion intercalation and laminate cation doping [16,17]. For example, Liu and colleagues reported a method to prepare ultrathin CoFe-LDH nanosheets with many cavities as OER electrocatalysts by plasma etching, which have more active sites and cavities than the original CoFe-LDH and thus achieving an overpotential of 232 mV at 10 mA cm⁻² [18]. M et al. synthesized NiFe-LDH nanosheets with different interlayer anions and

* Corresponding authors.

** Corresponding author at: Key Laboratory for Green Processing of Chemical Engineering of Xinjiang Bingtuan, School of Chemistry and Chemical Engineering, Shihezi University, Shihezi 832003, China

E-mail addresses: yangjinfeng@shzu.edu.cn (J. Yang), zhang_lili@isce2.a-star.edu.sg (L. Zhang), yufeng05@mail.ipc.ac.cn (F. Yu).

¹ These two authors contributed equally to this work.

found that the higher catalytic activity of NiFe-LDH with phosphate intercalation was attributed to the higher water oxidation activity of the nitrite species bound to the edge iron [19]. To achieve good catalytic performance, the number of active sites needs to be increased, the electronic properties need to be tuned, and the surface properties of the catalyst need to be tailored [20]. Typically, LDH consist of many layers stacked together, and thus only a limited number of active sites are accessible and being utilized [21].

Amorphous materials are widely used in catalysis due to their disordered atomic arrangement and unsaturated coordination. Compared with crystalline materials, amorphous materials do not have a periodic structure but consist of a continuous random network, and therefore exhibit some unique properties [22,23]. The fabrication and application of a large number of amorphous materials has been extensively studied in the past decades [24]. For example, J and his colleagues reported that the interaction between oxygen vacancies in Co_3O_4 and the amorphous region in NiFe-LDH coordinates the unsaturated Fe species, finally completing the electron backtracking, requiring only low overpotentials of 221 and 257 mV to provide current densities of 100 and 500 mA cm^{-2} respectively [25,26]. Zheng and his team fabricated wafer-sized amorphous PtSe_x films on SiO_2 substrates by a low-temperature amorphization strategy, which resulted in a layer of Pt single-atom with high atom-utilization efficiency [27]. U and Song used surface fluorination method to induce partial amorphization to form a high density crystal-amorphous interface. The partially amorphized Co_2B achieved 13% reduction in OER overpotential at 10 mA cm^{-2} compared to Co_2B crystals [28]. Hu et al. synthesized hybrid amorphous/crystalline FeCoNi-LDH loaded with monatomic Ru with abundant defects in the outer layer, which showed an overpotential of 205 mV at the current density of 10 mA cm^{-2} [29]. The flexible structure in amorphous phase can accelerate the transfer of electrons which are highly desirable in water electrolysis. However, current approaches generally require high temperature treatment or thin film technology (atomic layer deposition) [30]. Therefore, it is particularly important to develop a simple strategy to prepare efficient photoelectron-catalyst for water electrolysis [31].

Herein, a highly crystalline 2D ZnAl-LDH with good photoelectric response was first prepared using a co-precipitation method. Then, amorphous Si-doped ZnAl-LDH nanosheets (denoted as Si-ZnAl-LDH nanosheet: amorphous structure, no longer LDH structure) with large area and abundant catalytically active centers were achieved by chemical exfoliation of crystalline ZnAl-LDH by silicon tetrachloride. The thinning or layering of crystalline ZnAl-LDH into ultrathin amorphous Si-ZnAl-LDH nanosheet, as well as the introduction of Si lead to improved photoelectrocatalytic activity of water splitting. The incorporation of Si to highly exfoliated ZnAl-LDH nanosheets generates more oxygen vacancies, increases the number of active sites, enhance the local charge density of the active centers and effectively suppress the recombination of the generated electron-hole pairs. The degree of hybridization of s and p orbitals of Si-ZnAl-LDH nanosheet increases significantly, especially during the light irradiation (compared to that of crystalline ZnAl-LDH), which narrows the band gap so as to reduce the energy barrier. The effective energy band density becomes denser with the introduction of Si atoms, which can effectively activate the electrons and promote the electron transport. Therefore, more electrons can be excited to the conduction band, generating additional charge carriers and thus improving the charge transport properties and the overall photoelectrocatalytic activity. This opens a new strategy to prepare inexpensive and efficient photoelectrocatalytic materials for green energy production.

2. Experimental

2.1. Materials and synthesis of ZnAl-LDH and Si-ZnAl-LDH nanosheet

Zinc nitrate hexahydrate ($\text{Zn}(\text{NO}_3)_2 \cdot 6 \text{H}_2\text{O}$), aluminum nitrate

nonahydrate ($\text{Al}(\text{NO}_3)_3 \cdot 9 \text{H}_2\text{O}$), anhydrous sodium carbonate (Na_2CO_3), sodium hydroxide (NaOH), and silicon tetrachloride (SiCl_4) were purchased from McLean Corporation, and all reagents are of analytical grade and all chemicals are used as is, without further purification.

$\text{Zn}(\text{NO}_3)_2 \cdot 6 \text{H}_2\text{O}$ (12 mmol), $\text{Al}(\text{NO}_3)_3 \cdot 9 \text{H}_2\text{O}$ (6 mmol) and anhydrous Na_2CO_3 (6 mmol) were weighed and dissolved in 50 mL of deionized water, respectively, with stirring until the solution became transparent. The mixed solution of $\text{Zn}(\text{NO}_3)_2 \cdot 6 \text{H}_2\text{O}$ and $\text{Al}(\text{NO}_3)_3 \cdot 9 \text{H}_2\text{O}$ was then rapidly dripped into Na_2CO_3 solution. During this step, a certain amount of NaOH was used to adjust the pH at 9.5–10, and the solution was left for crystallization for 24 h with constant stirring. Then the mixture is transferred to an oven for aging at 80 °C for 24 h. Finally, the product was obtained by washing with deionized water and anhydrous ethanol until the filtrate was neutral. After drying in an oven at 80 °C for 24 h, the ZnAl-LDH was obtained by grinding.

0.2 g of ZnAl-LDH powder was placed in a certain amount of cyclohexane under stirring for 20 min. 4 mL of silicon tetrachloride solution was slowly added into the above mixture and stirred at room temperature for 24 h. After that, the solid was dried in an oven at 80 °C for 1 h, and ground to obtain amorphous Si-ZnAl-LDH nanosheet.

2.2. Catalyst characterization

Wide-angle XRD tests were performed using a D8 advanced instrument from Bruker, Germany, with Cu K α as the radiation source ($\lambda = 1.541 \text{ nm}$) and a cuvette current of 40 mA for the instrument. The scan range was set to 10°–70° (2 θ) and the scan rate was 5 °C/min. The microstructure, lattice stripes and SAED of the samples were observed using a transmission electron microscope (JEM 2100 F FEI Tecnai F20/F30). The thickness of the lamellae of the nanosheets was observed and analyzed by atomic force microscopy (AFM). The instrument model is Bruker Dension Icon. X-ray photoelectron spectroscopy (XPS) was performed with Thermo ESCALAB 250XI, Thermo Fisher Scientific. Sample optical properties were measured by UV-Vis spectrometer (UV-2600) in the light absorption range, and steady-state transient fluorescence spectrometer (FLS1000/FS5) is used to analyze the electron and hole complexes, as well as the fluorescence lifetime.

2.3. Electrochemical performance test

A standard three-electrode system (reference electrode: Ag/AgCl with saturated KCl (3.0 M) filling solution, counter electrode: graphite rod and working electrode: nickel foam loaded with active material) was tested using a CHI 760E electrochemical workstation in an O_2 -saturated 1 M KOH electrolyte. A CEL-HXF300 xenon lamp was used with a photocurrent value of 15 A and an optical power of 15.1 mW. The catalyst loading was 2 mg cm^{-2} and cyclic voltammetry (CV) scans were performed in the potential range 0–0.8 V (vs. Ag/AgCl) at a sweep rate of 50 mV s^{-1} until a stable, overlapping curve was obtained before data collection. Linear scans (LSV) were obtained by testing at a sweep rate of 1 mV s^{-1} over the same voltage range. To further investigate the electrocatalytic kinetics, electrochemical impedance spectroscopy (EIS) measurements were performed in the frequency range of 10 Hz to 0.01 kHz at an AC voltage of 5 mV, and their electrochemically active surface area (ECSA) was tested at different scan rates.

2.4. Theoretical calculations

Spin-polarized DFT calculations were performed using the quantum ATK platform and orbital linear combination correlation functions. For electron-ion interactions, the plane wave pseudopotential in the projection-enhanced (PAW) method was employed. The ZnAl-LDH catalyst surface was simulated by a ($3 \times 3 \times 1$) supercell with lattice parameters of $a = 15.98 \text{ \AA}$, $b = 10 \text{ \AA}$, and $c = 20 \text{ \AA}$. The Si-ZnAl-LDH nanosheet catalyst was constructed by replacing some hydrogen atoms of ZnAl-LDH with Si for ($3 \times 3 \times 1$) super-cell simulations with lattice

parameters of $a = 15.98 \text{ \AA}$, $b = 10 \text{ \AA}$ and $c = 20 \text{ \AA}$. A vacuum layer with a thickness of 15 \AA was added in the z-direction to prevent interactions between the periodic flat plate models in the xy-plane, and the geometry was optimized to control the convergence so that the maximum residual force was less than 0.02 eV/\AA . The Si-ZnAl-LDH nanosheet catalysts were also optimized by adding a vacuum layer in the z-direction of 15 \AA to prevent interactions between the periodic flat plate models in the xy-plane.

3. Results and discussion

3.1. Catalyst structure

A schematic diagram of the process of SiCl_4 exfoliation of ZnAl-LDH nanosheets by chemical method is shown in Fig. 1a. The powder XRD patterns of the catalysts are shown in Fig. 1b. The blue lines are ZnAl-LDH sheets prepared by co-precipitation method, and the diffraction angles of 11.6° , 23.4° , 34.6° , 39.2° , 60.1° , and 61.5° are the same as standard card (PDF#38-0486), corresponding to the characteristic peaks of (003), (006), (012), (015), (110), and (113) planes of crystalline ZnAl-LDH, respectively. No other impurity is found, indicating that the highly crystalline ZnAl-LDH was successfully prepared. The purple line indicates amorphous Si-ZnAl-LDH nanosheets after chemical exfoliation. It can be clearly observed that the diffraction peaks associated with crystalline ZnAl-LDH disappeared after the addition of SiCl_4 . The

lamellar thickness of ZnAl-LDH was measured by atomic force microscopy (AFM) as shown in Fig. 1c. The height of ZnAl-LDH sheet is very similar, while the height of Si-ZnAl-LDH nanosheets (Fig. 1d) after SiCl_4 exfoliation is inconsistent and covers a wide range from 1 nm to 35 nm . Drastic difference between crystalline ZnAl-LDH and amorphous Si-ZnAl-LDH nanosheets can be clearly seen under TEM (Fig. 1e vs 1i). The crystalline ZnAl-LDH sheet has the typical dense hexagonal structure (Fig. 1g); while amorphous Si-ZnAl-LDH nanosheet shows three-dimensional sphere-like structure consisting of much thinner nanosheets after chemical exfoliation (Fig. 1i). The change of ZnAl-LDH morphology from hexagonal structure to sphere-like structure can be explained by the following: chemical exfoliation of crystalline ZnAl-LDH by SiCl_4 results in the formation of amorphous ZnAl-LDH nanosheets that quickly or spontaneously self-assembled into three-dimensional sphere-like nanostructure to minimize the total surface energy. Fig. 1j shows bright and varying colors of the amorphous Si-ZnAl-LDH nanosheets, which verifies the 3D structure from the self-assembly of the Si-ZnAl-LDH nanosheets. HRTEM image of ZnAl-LDH have clear lattice spacing of 0.299 nm , 0.264 nm , and 0.259 nm , corresponding to the (110), (101), and (012) crystal planes of ZnAl-LDH, respectively (Fig. 1g). The diffraction apertures consisting of (110), (101) crystalline planes and (015) crystalline planes were found in the SAED map of ZnAl-LDH (Fig. 1h), further confirming the highly crystalline nature of the ZnAl-LDH materials. On contrast, HRTEM (Fig. 1k) does not show any lattice stripes and no diffraction aperture in SAED map (Fig. 1l),

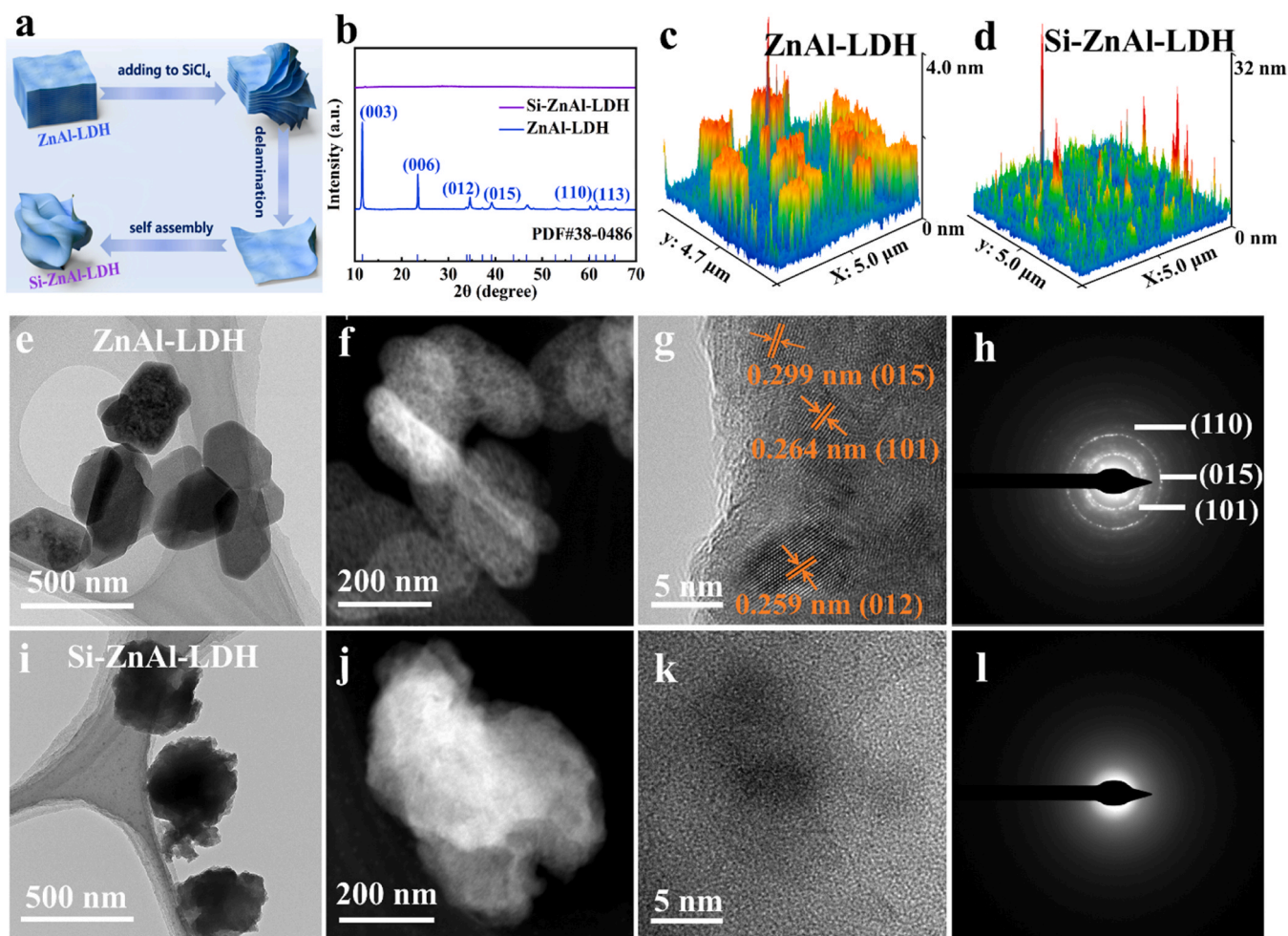


Fig. 1. (a) Schematic diagram of the process of exfoliating ZnAl-LDH nanosheets by SiCl_4 , (b) XRD Patterns of ZnAl-LDH, Si-ZnAl-LDH nanosheet and Standard cards (PDF#38-0486), (c) AFM results of (c) ZnAl-LDH and (d) Si-ZnAl-LDH nanosheet, (e) TEM image of ZnAl-LDH, (f) STEM-HAADF image of ZnAl-LDH, (g) HRTEM image of ZnAl-LDH, (h) SAED pattern, (i) TEM image of Si-ZnAl-LDH nanosheet, (j) STEM-HAADF images of Si-ZnAl-LDH nanosheet, (k) HRTEM images of Si-ZnAl-LDH nanosheet, and (l) SAED pattern.

indicating amorphous nature of Si-ZnAl-LDH nanosheets. The formation of amorphous ZnAl-LDH nanosheets through exfoliation leads to much more accessible surfaces that originally are not accessible in highly crystalline ZnAl-LDH sheets. This enhances the exposure of the active sites so as to increase the contact between the active sites and the reactants. Hence, more favorable catalytic activity is expected for amorphous Si-ZnAl-LDH nanosheet catalyst.

To understand the chemical state of the catalyst surface, photoelectron spectroscopy (XPS) under light was performed. As shown in Fig. 2b, the characteristic peaks of Zn $2p_{3/2}$ and Zn $2p_{1/2}$ appeared at 1022.3 eV and 1045.4 eV, with little shift in the binding energy of each sub-peak during and after the light exposure (compared to the pre-light exposure). On the other hand, Zn 2p of the Si-ZnAl-LDH nanosheet sample (Fig. 2f) before light irradiation is shifted to a higher binding energy comparing to that of ZnAl-LDH, indicating that there is a certain degree of unsaturation of Zn due to the incorporation of Si [32]. The shift towards higher binding energies for all subpeaks during light exposure is caused by the adsorption of OH* species during light exposure [33], where oxygen vacancies in the surface layer dissociate water through the transfer of a proton to a nearby oxygen atom, forming two OH* per vacancy, and the rapidity of water dissociation is limited by the number of oxygen vacancies on the surface [34]. There is no doubt that the incorporation of Si and the exfoliation process leads to the formation of more oxygen vacancies, which become more prominent during illumination and therefore exhibit better photo responses.

The Al 2p spectra of ZnAl-LDH sample (Fig. 2c) at binding energies of 74.1 eV and 74.9 eV are attributed to Al in Al-OH and Al-O bonds. These two binding energies are shifted towards lower values with light, implying that Al gains electrons during the light exposure. The electron density increases, Al³⁺ is reduced to Al²⁺ and H* is activated [33]. After the end of the illumination, the subpeaks are shifted toward higher binding energy (relative to the illumination period) and almost go back to the pre-illumination binding energy. This result indicates the recombination of the electron-hole pairs, which is not favorable for the photocatalytic reaction. The XPS pattern of Al 2p for the Si-ZnAl-LDH nanosheet sample is shown in Fig. 2g, with only one subpeak attributed to Al-O is observed instead of two. During the light exposure, the binding energy shifted toward higher binding energies, suggesting a possible conversion in the form of active H* species in the case of adsorbed intermediate species. This will induce electrons on Al to

promote the decomposition of water. At the end of the light exposure, the binding energy (relative to the light exposure period) did not shift, indicating that the electron-hole pairs did not combine [35], which facilitates the photocatalytic reaction.

The O 1s XPS diagrams of ZnAl-LDH and Si-ZnAl-LDH nanosheet can be deconvoluted into three sub-peaks at binding energies of 531.57 eV, 532.6 eV, and 533.5 eV, corresponding to metal oxygen (oxygen atoms bonded to metals), Vo (defect sites with low oxygen coordination) and the adsorbed molecular water [36,37], respectively. The O1s binding energy of the Si-ZnAl-LDH nanosheet sample (Fig. 2h) shifted significantly towards high binding energy relative to that of the ZnAl-LDH sample (Fig. 2d) before illumination, attributed to the incorporation of Si. The Si-ZnAl-LDH nanosheet showed almost no change in Vo peak area (remain at about 31%) at the end of the light irradiation, while the Vo peak area of ZnAl-LDH sample significantly decreased from 31% during the light illumination to 23% at the end of the light irradiation. Electron Paramagnetic Resonance (EPR) were conducted to prove the presence of oxygen vacancies and is shown in Fig. S5. Increased oxygen vacancies on Si-ZnAl-LDH nanosheet sample is clearly seen during light illumination. Oxygen vacancies are vacancies left by the absence of oxygen atoms in the material, and they are usually considered as active sites in the catalytic process. The introduction of Si increased the number of these active sites, which may help to improve the activity of the catalyst [38]. For oxygen atoms bonded to metals, sample ZnAl-LDH showed almost no change in peak area before, during, and after light exposure; while for Si-ZnAl-LDH nanosheet sample, the peak area became significantly smaller during light exposure compared to (before) light exposure, which is due to the amorphous structure of Si-ZnAl-LDH nanosheet sample. The self-reconfiguration during illumination leads to the bonding of Al-O to its Si, forming more Si-O-Al bonds, which is consistent with the XPS results of Si 2p below. Meanwhile, in terms of adsorbed molecular water fractionation, the fractionation areas of both ZnAl-LDH and Si-ZnAl-LDH nanosheet samples increased after the introduction of light, indicating that light is favorable for water adsorption. The increase in adsorbed water is obviously much more for sample Si-ZnAl-LDH nanosheet with light, and the involvement of Si generates more oxygen vacancies during the light illumination, which further enhance water adsorption by the catalyst. It is clear that the amorphous Si-ZnAl-LDH nanosheet sample has abundant catalytically active phases Al-O-Si, thus is favorable for photocatalytic activity.

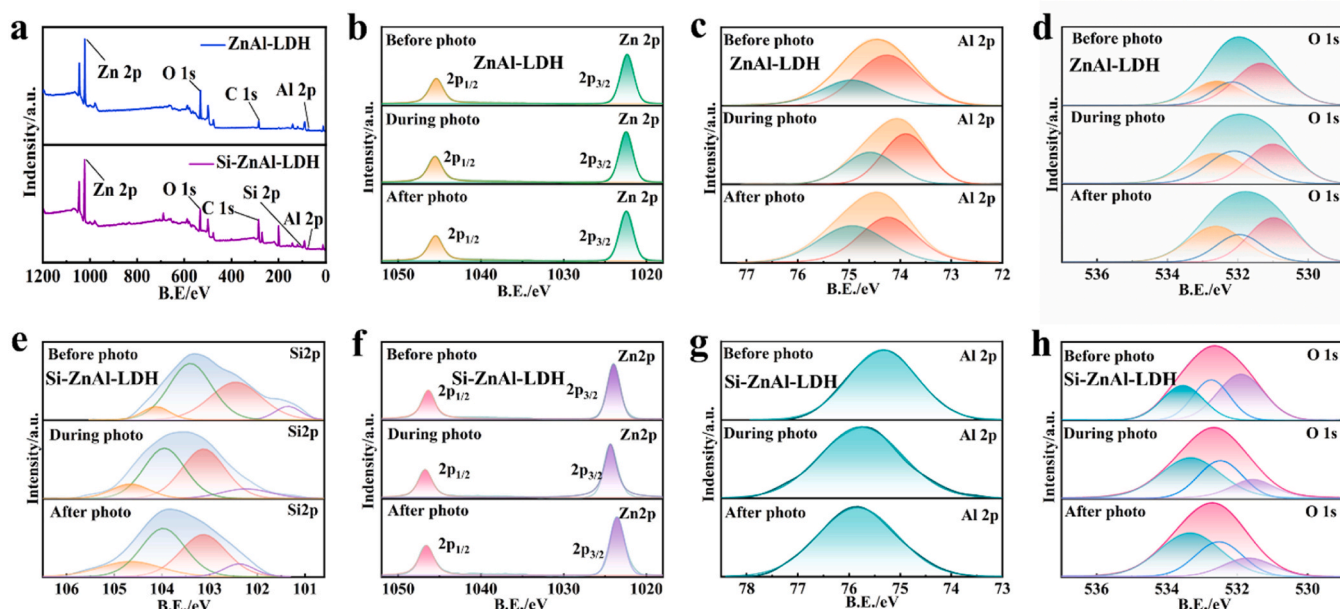


Fig. 2. XPS spectra of (a) wide scan spectra, comparison of XPS spectra of the ZnAl-LDH, Si-ZnAl-LDH nanosheet (b), (f) Zn 2p, (c), (g) Al 2p, (d), (h) O 1s, (e) Si 2p.

Si 2p spectrum of Si-ZnAl-LDH nanosheet before illumination (Fig. 2e) has binding energies at 101.3 eV, 102.5 eV, 103.2 eV, 104.1 eV, corresponding to SiO_x [39], $\text{SiO}_2(\text{Al}_2\text{O}_3)_{0.22}$, [40] $\text{Al}_{0.2}\text{Si}_{0.8}\text{O}_{2.2}$ [41] and O_2/Si [42], respectively. The binding energies of all subpeaks of the Si 2p spectrum shifted toward higher binding energy during the illumination period, and the binding energy of SiO_x shifted from 101.3 eV to 102.2 eV. Such a large shift may be attributed to the enhanced oxidation state of Si during the light illumination to form $\text{SiO}_2(\text{Al}_2\text{O}_3)_{0.55}$ species, and the binding energy of SiO_x of 102.2 eV after the illumination was attributed to $\text{SiO}_2(\text{Al}_2\text{O}_3)_{0.55}$ species. The emergence of $\text{SiO}_2(\text{Al}_2\text{O}_3)_{0.55}$ species is a result of the self-reconfiguration of Si-ZnAl-LDH nanosheet during light exposure. The relative decrease in peak area of $\text{SiO}_2(\text{Al}_2\text{O}_3)_{0.55}$ species is due to decrease in the Si content of the higher valence state with the disappearance of light. The binding energies of the $\text{SiO}_2(\text{Al}_2\text{O}_3)_{0.22}$ and $\text{Al}_{0.2}\text{Si}_{0.8}\text{O}_{2.2}$ were found to be unshifted. The above results indicate that light can induce Si to form more active substances that can participate in the catalytic reaction.

Based on the above characterizations and analysis, the transformation of ZnAl-LDH structure into amorphous Si-ZnAl-LDH nanosheets through chemical exfoliation is summarized below. The reaction between SiCl_4 and ZnAl-LDH involves the interaction of Cl with hydrogen on -OH to form HCl, and Si with oxygen on -OH to form Al-O-Si covalent bonds. The presence of various Al-O-Si species (such as $\text{SiO}_2(\text{Al}_2\text{O}_3)_{0.22}$, $\text{Al}_{0.2}\text{Si}_{0.8}\text{O}_{2.2}$, $\text{SiO}_2(\text{Al}_2\text{O}_3)_{0.55}$) are shown in XPS in Fig. 2. The HCl formed during the process etches ZnAl-LDH, while the incorporation of Si causes the expansion of the LDH layer spacing and thus weakens the interaction between the layers, leading to the exfoliation of LDH into nanosheet structure. The exfoliation and corrosion introduces defects and irregular arrangement of the nanosheets leads to the final amorphous ZnAl-LDH nanosheets which are confirmed by XRD (Fig. 1b), TEM (Fig. 1i), STEM-HAADF (Fig. 1j) and HRTEM (Fig. 1k).

To compare the optical properties of the two catalysts and to reveal the role of light in the catalyst performance, a series of optical properties were characterized. The Mott Schottky curves of the ZnAl-LDH and amorphous Si-ZnAl-LDH nanosheet samples are shown in Fig. 3a. The amorphous Si-ZnAl-LDH nanosheet catalyst shows a smaller slope of the inverse of the capacitance versus the applied potential compared to that of the ZnAl-LDH catalyst. Therefore, Si-ZnAl-LDH nanosheet offers a larger charge carrier density. To evaluate the photogenerated charge separation efficiency of the catalysts, photoluminescence (PL) spectra were tested (Fig. 3b). The PL spectra showed that Si-ZnAl-LDH

nanosheet has significantly lower depth-defect emission and lower recombination rate of hole pairs compared to that of ZnAl-LDH. This result indicates that the former can generate more effective photo-generated carriers to participate in photochemical conversion. The longer the carrier lifetime, the higher the possibility of participating in the photocatalytic reaction. Therefore, the photogenerated carrier lifetimes of samples ZnAl-LDH and Si-ZnAl-LDH nanosheet were further investigated by the time-resolved PL spectra and results are shown in Fig. 3c. The short lifetime component (τ_1) of ZnAl-LDH and Si-ZnAl-LDH nanosheet was 0.13 ns and 0.5 ns, respectively. The extended lifetime for amorphous Si-ZnAl-LDH nanosheet indicates that the incorporation of Si and the chemical exfoliation prolonged the charge carrier's lifetime and suppressed the electron-pair recombination. Meanwhile, the long lifetime component (τ_2) of ZnAl-LDH was 1.21 ns, while that of amorphous Si-ZnAl-LDH nanosheet increased nearly twofold to 2.41 ns. This indicates a faster and more efficient charge transfer under the light condition. The incorporation of Si resulted in longer lifetime components than that of ZnAl-LDH, suggesting that amorphous Si-ZnAl-LDH nanosheet has higher separation efficiency thus increasing the probability of carrier participation in the allytic water reaction process and further improving the photocatalytic performance. The transient photocurrent spectra were shown in Fig. 3d, and Si-ZnAl-LDH nanosheet exhibited higher photocurrent intensity under illumination, indicating its higher transfer efficiency and stronger light trapping ability.

The UV-Vis diffuse reflectance spectra of the ZnAl-LDH and Si-ZnAl-LDH nanosheet samples are shown in Fig. 3e. It is observed that the absorption edge of the ZnAl-LDH catalyst is about 350 nm, while that of the Si-ZnAl-LDH nanosheet catalyst is significantly red-shifted and the absorption edge expands to near 410 nm. The Tauc plot of UV-Vis absorption spectrum in Fig. 3f was obtained by Kubelka-Munk function conversion, and the results showed that the band gap of ZnAl-LDH and Si-ZnAl-LDH nanosheet was 3.09 eV and 2.25 eV, respectively. The band gap energy of Si-ZnAl-LDH nanosheet was reduced compared with the original ZnAl-LDH, and the narrower band gap can promote the electron leaving domain and photoexcited charge migration, which has a significant effect on the photocatalytic efficiency. The valence band values of the ZnAl-LDH and Si-ZnAl-LDH nanosheet catalysts is found to be 3.7 eV and 3.14 eV, respectively (Fig. 3g). The energy band structures of the two catalysts were also calculated based on the valence band values and band gaps as shown in Fig. 3h. The conduction band potential (CB) of Si-ZnAl-LDH nanosheet was found to be more negative than the HER

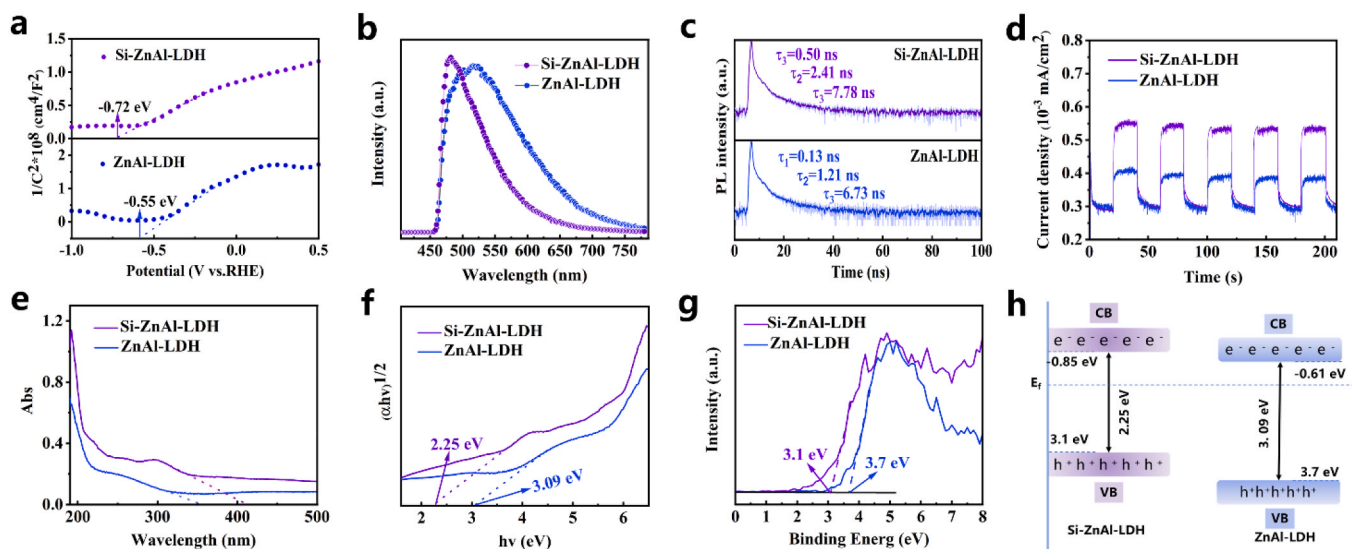


Fig. 3. Comparison of Optical property of the Si-ZnAl-LDH nanosheet, ZnAl-LDH (a) Model Schottky plot, (b) PL spectra, (c) TRPL decay curve, (d) photocurrent curves, Comparison of Energy band structure of the Si-ZnAl-LDH nanosheet, ZnAl-LDH (e) UV-vis diffuse reflectance spectra, (f) Tauc plots of the UV-vis absorption spectra, (g) UV-XPS spectra, (h) energy band diagram of Si-ZnAl-LDH nanosheet and ZnAl-LDH.

theoretical potential (0 V vs. RHE), and the valence band potential (VB) was found to be more positive than the OER theoretical potential (1.23 V vs. RHE). It indicates that the material is theoretically good for both HER and OER reactions. Based on the above results, Si-ZnAl-LDH nanosheet has a wider light absorption range and photo-responsiveness than ZnAl-LDH.

3.2. Electrochemical performances of the catalyst

The light-assisted electrochemical performance of ZnAl-LDH and Si-ZnAl-LDH nanosheet was tested under 1.0 M KOH conditions using a standard three-electrode test system (Light stands for light irradiation conditions, abbreviated as L; Dark stands for no light irradiation conditions, abbreviated as D). After cyclic voltammetry (CV) scanning, linear scanning voltammetry (LSV) curves were obtained at 1 mV s^{-1} as represented in Fig. 4a for the HER reaction. The overpotential of the ZnAl-LDH catalyst under light irradiation decreased from 180 mV to 130 mV at a current density of -10 mA cm^{-2} . The Si-ZnAl-LDH nanosheet catalyst under dark had an overpotential of 140 mV at current density- 10 mA cm^{-2} , 40 mV lower than that of ZnAl-LDH catalyst. Under light irradiation, the overpotential of the Si-ZnAl-LDH nanosheet catalyst was only 108 mV at current density- 10 mA cm^{-2} . The Tafel slope was obtained by extrapolating the LSV curve and is shown in Fig. 4b. The Si-ZnAl-LDH nanosheet catalyst had the smallest Tafel slope of $113.2 \text{ mV dec}^{-1}$, indicating that it has the fastest HER kinetic behavior and mass transfer rate. The charge transfer resistance of the samples was evaluated by photoelectrochemical impedance spectroscopy (PEIS) at overpotential of 200 mV for HER (Fig. 4c) while PEIS at open circuit potential is shown in Fig.S8. Si-ZnAl-LDH nanosheet in light exhibited the smallest arc radius, indicating that the charge carrier resistance was the smallest under light. HER stability of the Si-ZnAl-LDH

nanosheet catalyst at a current density of -10 mA cm^{-2} was evaluated using the constant current measurement chrono-potential (CP) method (Fig. 4d). The Si-ZnAl-LDH nanosheet catalyst under light irradiation was 330 mV at a current density of 10 mA cm^{-2} , 30 mV lower than that of ZnAl-LDH catalyst. Under light irradiation, the overpotential of Si-ZnAl-LDH nanosheet catalyst was only further reduced to 260 mV at the current density of -10 mA cm^{-2} . Similarly, the smallest Tafel slope (86 mV dec^{-1}) and smallest charge transfer resistance was obtained for Si-ZnAl-LDH nanosheet catalysts. PEIS of the catalysts with and without light at overpotential of 300 mV for OER are shown in Fig. 4g. The diameter of the semicircle is related to the charge transfer resistance at the electrode-electrolyte interface, and Si-ZnAl-LDH nanosheet exhibits a smaller arc radius than that of ZnAl-LDH, especially under light illumination, indicating a relatively faster charge transfer rate and better kinetics under light illumination. The OER stability of the Si-ZnAl-LDH nanosheet catalyst at a current density of 10 mA cm^{-2} was evaluated (Fig. 4h) and no decay in catalytic performance was observed.

In order to further investigate the effect of different Si doping on the performance of HER and OER, we have varied the Si doping level from 0.5:1 to 2:1, and the results are shown in Fig. S6. The sample with 1:1 ratio exhibits the best photocatalytic results. This is due to the interaction between the dopant and the raw material (ZnAl LDH) is the optimum at 1:1 ratio. At the ratio of 1:1, the Si is well coordinated with ZnAl-LDH to produce the most number of active sites; whereas at the ratio of 0.5:1, there is insufficient exfoliation, resulting in too few exposed active

nanosheet catalyst at a current density of -10 mA cm^{-2} was evaluated using the constant current measurement chrono-potential (CP) method (Fig. 4d). The Si-ZnAl-LDH nanosheet catalyst under light irradiation was 330 mV at a current density of 10 mA cm^{-2} , 30 mV lower than that of ZnAl-LDH catalyst. Under light irradiation, the overpotential of Si-ZnAl-LDH nanosheet catalyst was only further reduced to 260 mV at the current density of -10 mA cm^{-2} . Similarly, the smallest Tafel slope (86 mV dec^{-1}) and smallest charge transfer resistance was obtained for Si-ZnAl-LDH nanosheet catalysts. PEIS of the catalysts with and without light at overpotential of 300 mV for OER are shown in Fig. 4g. The diameter of the semicircle is related to the charge transfer resistance at the electrode-electrolyte interface, and Si-ZnAl-LDH nanosheet exhibits a smaller arc radius than that of ZnAl-LDH, especially under light illumination, indicating a relatively faster charge transfer rate and better kinetics under light illumination. The OER stability of the Si-ZnAl-LDH nanosheet catalyst at a current density of 10 mA cm^{-2} was evaluated (Fig. 4h) and no decay in catalytic performance was observed.

In order to further investigate the effect of different Si doping on the performance of HER and OER, we have varied the Si doping level from 0.5:1 to 2:1, and the results are shown in Fig. S6. The sample with 1:1 ratio exhibits the best photocatalytic results. This is due to the interaction between the dopant and the raw material (ZnAl LDH) is the optimum at 1:1 ratio. At the ratio of 1:1, the Si is well coordinated with ZnAl-LDH to produce the most number of active sites; whereas at the ratio of 0.5:1, there is insufficient exfoliation, resulting in too few exposed active

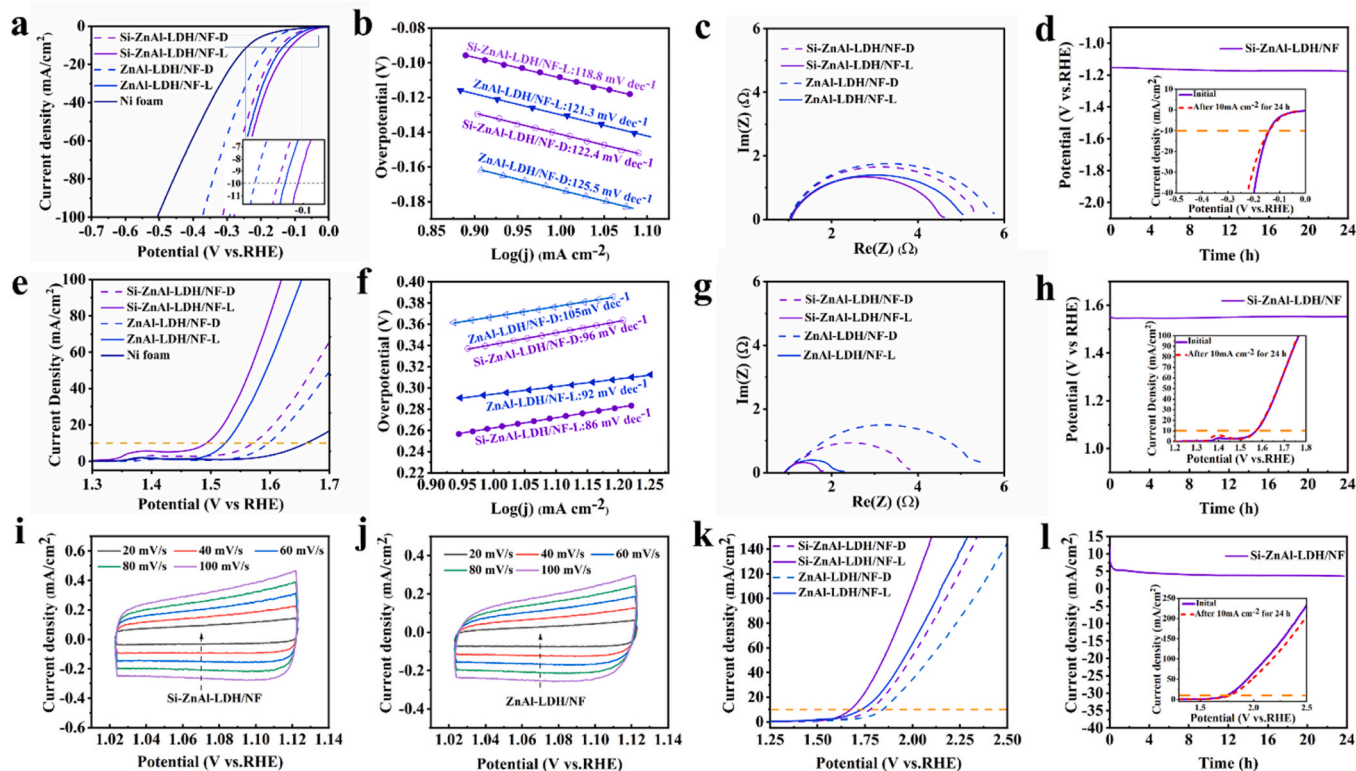


Fig. 4. HER performance (a) LSV curves, (b) Tafel slope, (c) Impedance spectroscopy at overpotential of 200 mV for HER, (d) Long-term stability test (inset: Comparison of HER overpotential and initial value after stability test). OER performance (e) LSV curves, (f) Tafel slope, (g) Impedance spectroscopy at overpotential of 300 mV for OER, (h) Long-term stability test (inset: Comparison of OER overpotential and initial value after stability test). CV curves of (i) Si-ZnAl-LDH nanosheet and (j) ZnAl-LDH at different scan rates, Overall water splitting of Si-ZnAl-LDH nanosheet (k) LSV curves, (l) Durability test (inset: before and after the durability test).

sites. On the contrary, a 2:1 ratio may lead to too much Si complex, which covers the active sites after exfoliation, leading to poor catalytic effect.

The double layer capacitance (C_{dl}) measurements were performed for two samples with a voltage window of 0.1–0.2 V and a scan rate of $20 \text{ mV s}^{-1} \sim 100 \text{ mV s}^{-1}$. It can be seen from Fig. 4i and Fig. 4j that the integrated area of the CV curves increases with increasing scan rate. The Si-ZnAl-LDH nanosheet catalyst has the largest ECSA value as estimated by the bilayer capacitance, which means that it has the largest catalytic active site in the OER reaction compared to the ZnAl-LDH catalyst. Due to more catalytic active sites, the hydroxyl groups are more easily adsorbed, thus increasing the electron transfer efficiency between the electrode surface and the electrolyte. In order to understand the performance of Si-ZnAl-LDH nanosheet samples in real hydrolysis, we performed the test of full hydrolysis in a double-chamber electrolytic cell. The LSV curves of Si-ZnAl-LDH nanosheet as cathode and anode were collected at a scanning rate of 5 mV s^{-1} . As can be seen in Fig. 4k, the applied potential of the Si-ZnAl-LDH nanosheet catalyst of the same material decreases from 1.733 V to 1.672 V after the addition of light. The long-term stability of Si-ZnAl-LDH nanosheet was tested for 24 h at a cell voltage of 1.8 V. The current density (Fig. 4l) was maintained at about 5 mA cm^{-2} and showed good stability. Coupling light with water electrolysis provides synergistic effect, which can not only significantly reduce the applied voltage, but also utilize natural light to improve the overall efficiency of hydrogen production.

3.3. Charge distributions and Gibbs free energy by density functional theory

The charge distributions of ZnAl-LDH and Si-ZnAl-LDH nanosheet were further analyzed using density functional theory (DFT) calculations. Under the dark conditions, as shown in Fig. 5a and c, the introduction of Si led to the local charge redistribution of LDH. The newly formed electron cloud distribution was expanded, resulting in a more uniform distribution of electrons in the material. The charge redistribution process significantly improves the electrical conductivity, catalytic activity and other properties of the material. Under light irradiation condition as shown in Fig. 5b and d, the electron cloud density further decreases, indicating that the introduction of light promotes the excitation of charge and the separation of effective charge. The projected density of states (PDOS) results show that Si-ZnAl-LDH nanosheet has a narrower band gap than ZnAl-LDH under dark reaction conditions as in Fig. 5e and g. As can be seen in Fig. 5g, the introduction of Si brings the conduction band (CB) and valence band (VB) closer to the Fermi energy level with enhanced hybridization of S and P orbitals. As the band gap narrows, the energy barrier required for electron transfer from the valence band to the conduction band is reduced. As a result, more electrons can be excited to the conduction band, generating additional charge carriers and thus improving the charge transport properties. At the same time, electrons in the conduction band can move through the material more easily, exhibiting higher electron mobility and further improving the conductivity and electrochemical properties of the material. Under photo-responsive conditions, as illustrated in Fig. 5f and 5h, a reduction in the peak density of electron states near the Fermi energy level is observed. This decrease indicates an enhancement in electron delocalization and conductivity, favoring efficient electron transport and further facilitating the transition of electrons from the valence band (VB) to the conduction band (CB). The electron distribution near the Fermi surface plays a decisive role in the optoelectronic properties of semiconductor materials. It can be concluded that more carriers are transferred from the top of the valence band to the bottom of the conduction band under photoreaction conditions, which results in light absorption and improves the photocatalytic activity of the reaction.

Fig. 5(i-l) shows the effective energy bands under the dark reaction and light reaction conditions. Under the dark reaction conditions, the effective energy band density becomes denser with the introduction of Si

atoms, which can effectively activate the electrons and promote the electron transport. Under the light reaction conditions, the density of the effective energy band becomes even denser compared to the dark reaction. The introduction of light, which injects energy into electrons, accelerates electron migration while the dense energy band structure effectively reduces the excitation energy required for electron leap.

Meanwhile, to further investigate the HER and OER mechanisms of ZnAl-LDH and Si-ZnAl-LDH nanosheet, the Gibbs free energy barriers required for the HER and OER processes under photoreaction and dark reaction conditions were simulated by DFT calculations. The HER processes of the catalysts are shown in Fig. 5m and 5o. Under dark reaction conditions, Si-ZnAl-LDH nanosheet exhibits a rather low Gibbs free energy barrier, $\Delta G = 0.86 \text{ eV}$. The results indicate that the doping of Si in ZnAl-LDH can significantly improve the reaction kinetics of HER. Meanwhile, the Gibbs free energy barrier of Si-ZnAl-LDH nanosheet decreases to $\Delta G = 0.39 \text{ eV}$ under photoreaction conditions, indicating that Si-ZnAl-LDH nanosheet under photoreaction has a stronger hydrogen adsorption behavior and lower H_2 generation and desorption barriers, which makes it easier to undergo HER reaction. The OER reaction process ($U=0$) is shown in Fig. 5n and p. Under dark reaction conditions, the maximum Gibbs free energy barrier of ZnAl-LDH is $\Delta G_3 = 2.27 \text{ eV}$, corresponding to $\eta_{\text{OER}} = 1.123 \text{ V}$. This means that the strong adsorption of OOH^* species on ZnAl-LDH is the step that determines the reaction rate during the OER process. Additionally, although the rate-determining step of Si-ZnAl-LDH nanosheet remains unchanged, the Gibbs free energy decreases to 1.95 eV , resulting in a significant reduction of η_{OER} to 0.72 V . This indicates that the introduction of Si lowers the overpotential of OER by reducing energy required for the formation of OOH^* . Under light-responsive conditions, the maximum Gibbs free energy of ZnAl-LDH (ΔG_3) is 1.76 eV , corresponding to η_{OER} of 0.53 V . The introduction of light allows for more electrons to be excited to the conduction band, generating additional charge carriers participating in the reaction, thereby further reducing the energy barrier required for the rate-determining step. For Si-ZnAl-LDH nanosheet, $\Delta G_3 = 1.59 \text{ eV}$ serves as the rate-determining step, and compared to the dark reaction, η_{OER} decreases significantly to 0.36 V . The introduction of Si atoms leads to a significant narrowing of the band gap in the material. Under light conditions, more electrons can be excited to the conduction band, generating additional charge carriers and improving charge transfer. Simultaneously, the injection of extra energy into the electrons accelerates their migration.

4. Conclusions

In this study, ZnAl-LDH with photoresponsiveness were prepared by co-precipitation method and the Si doped ZnAl-LDH nanosheets were obtained through chemical exfoliation with SiCl_4 . The exfoliated amorphous Si-ZnAl-LDH nanosheets can not only improve the light absorption efficiency but also enhances the overall photoelectron responsiveness. The overpotential is only 108 mV and 260 at a current density of 10 mA cm^{-2} for HER and OER, respectively. A voltage of only 1.672 V is required to drive water decomposition under light assistance. We have shown both experimentally and theoretically that the improved photoelectrocatalytic activity of amorphous Si-ZnAl-LDH nanosheet is due to 1) the formation of amorphous ZnAl-LDH nanosheets through chemical exfoliation or layer engineering leads to much more accessible surfaces that originally are not accessible in highly crystalline ZnAl-LDH sheets 2) the incorporation of Si generates more oxygen vacancies, increases the number of active sites, redistribute the local charge density of the system and effectively suppress the recombination of the generated electron-hole pairs 3) the electron cloud density of Si-ZnAl-LDH nanosheet expands significantly and the electron transfer rate becomes faster 4) the degree of hybridization of s and p orbitals of Si-ZnAl-LDH nanosheet increases significantly during the light irradiation (compared to that of crystalline ZnAl-LDH), which narrows the band gap so as to reduce the energy barrier. As a result, more electrons can be

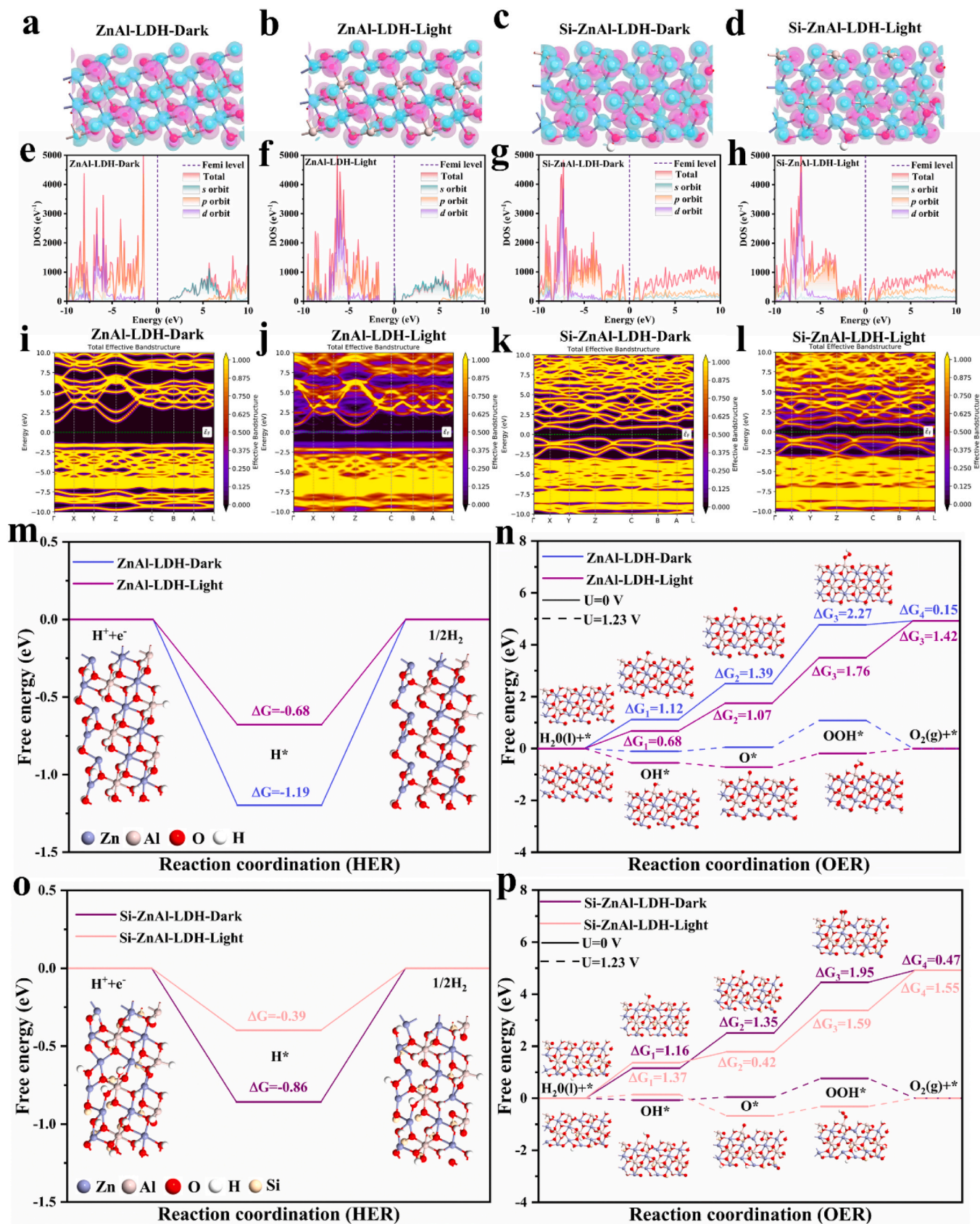


Fig. 5. (a-d) charge density differences, (e-h) projected DOS, (i-l) effective band structures under dark and light conditions. Fermi levels are at 0 eV, (m, o) HER Gibbs free energy diagram under dark and light conditions, (n, p) OER Gibbs free energy diagram under dark and light conditions.

excited to the conduction band, generating additional charge carriers and thus improving the charge transport properties and the overall photoelectrocatalytic activity.

CRedit authorship contribution statement

Wang Chenxu: Conceptualization, Validation. **Yan Wenxia:** Conceptualization, Validation. **Li Yangyang:** Conceptualization, Validation. **Bao Wentao:** Conceptualization, Data curation, Formal analysis, Investigation, Validation, Visualization, Writing – original draft. **Yu Jie:** Conceptualization, Validation. **Tang Ying:** Conceptualization, Formal analysis, Software. **Yang Jinfeng:** Conceptualization, Investigation, Writing – review & editing. **Wang Zhimou:** Conceptualization, Validation. **Yu Feng:** Conceptualization, Data curation, Formal analysis, Funding acquisition, Investigation, Validation, Visualization, Writing – review & editing. **Zhang Lili:** Conceptualization, Formal analysis, Funding acquisition, Writing – review & editing.

Declaration of Competing Interest

The authors declare that they have no known competing financial interests or personal relationships that could have appeared to influence the work reported in this paper.

Data Availability

Data will be made available on request.

Acknowledgment

This work was financially supported by Bingtuan Science and Technology Program (No. 2023AB033), Shihezi Science and Technology Program (No. 2023PT01), Central Research Fund, Agency for Science, Technology and Research (A*STAR).

Appendix A. Supporting information

Supplementary data associated with this article can be found in the online version at doi:10.1016/j.apcatb.2024.123706.

References

- [1] C. Liang, P. Zou, A. Nairan, Y. Zhang, J. Liu, K. Liu, S. Hu, F. Kang, H.J. Fan, C. Yang, Exceptional performance of hierarchical Ni-Fe oxyhydroxide@NiFe alloy nanowire array electrocatalysts for large current density water splitting, *Energy Environ. Sci.* 13 (1) (2020) 86.
- [2] J. Liu, X. Ji, J. Shi, L. Wang, P. Jian, X. Yan, D. Wang, Experimental and theoretical investigation of the tuning of electronic structure in SnO₂ via Co doping for enhanced styrene epoxidation catalysis, *Catal. Sci. Technol.* 12 (5) (2022) 1499.
- [3] J. Yu, F. Yu, M.-F. Yuen, C. Wang, Two-dimensional layered double hydroxides as a platform for electrocatalytic oxygen evolution, *J. Mater. Chem. A* 9 (15) (2021) 9389.
- [4] W. Wang, Z. Wang, Y. Hu, Y. Liu, S. Chen, A potential-driven switch of activity promotion mode for the oxygen evolution reaction at Co₃O₄/NiOxHy interface, *eScience* 2 (4) (2022) 438.
- [5] X. Guo, X. Wan, Q. Liu, Y. Li, W. Li, J. Shui, Phosphated IrMo bimetallic cluster for efficient hydrogen evolution reaction, *eScience* 2 (3) (2022) 304.
- [6] C. Dong, X. Liu, X. Wang, X. Yuan, Z. Xu, W. Dong, M.S. Riaz, G. Li, F. Huang, Hierarchical Ni/NiTiO₃ derived from NiTi LDHs: a bifunctional electrocatalyst for overall water splitting, *J. Mater. Chem. A* 5 (47) (2017) 24767.
- [7] Y. Zhou, H.J. Fan, Progress and challenge of amorphous catalysts for electrochemical water splitting, *ACS Mater. Lett.* 3 (1) (2020) 136.
- [8] Y. Wu, X. Liu, H. Zhang, J. Li, M. Zhou, L. Li, Y. Wang, Atomic sandwiched p-n Homojunctions, *Angew. Chem. Int. Ed.* 60 (7) (2021) 3487.
- [9] J. Di, J. Xiong, H. Li, Z. Liu, Ultrathin 2D photocatalysts: electronic-structure tailoring, hybridization, and applications, *Adv. Mater.* 30 (1) (2018) 1704548.
- [10] J. Yu, Z. Liu, F. Yu, W. Bao, B. Peng, G. Wang, L. Zhang, Y. Xu, F. Wang, Enhanced photoelectrochemical performance of ZnO/NiFe-layered double hydroxide for water splitting: experimental and photo-assisted density functional theory calculations, *J. Colloid Interface Sci.* 623 (2022) 285.
- [11] Y. Huang, S.L. Zhang, X.F. Lu, Z.P. Wu, D. Luan, X.W.D. Lou, Trimetallic Spinel NiCo₂Fe₂O₄ Nanoboxes for Highly Efficient Electrocatalytic Oxygen Evolution, *Angew. Chem. Int. Ed.* 60 (21) (2021) 11841.
- [12] L. Hui, Y. Xue, B. Huang, H. Yu, C. Zhang, D. Zhang, D. Jia, Y. Zhao, Y. Li, H. Liu, et al., Overall water splitting by graphdiyne-exfoliated and -sandwiched layered double-hydroxide nanosheet arrays, *Nat. Commun.* 9 (1) (2018) 5309.
- [13] Y. Zhao, X. Zhang, X. Jia, G.I.N. Waterhouse, R. Shi, X. Zhang, F. Zhan, Y. Tao, L.-Z. Wu, C.-H. Tung, et al., Sub-3 nm ultrafine monolayer layered double hydroxide nanosheets for electrochemical water oxidation, *Adv. Energy Mater.* 8 (18) (2018) 1703585.
- [14] Y. Wang, S. Wang, Z.L. Ma, L.T. Yan, X.B. Zhao, Y.Y. Xue, J.M. Huo, X. Yuan, S. N. Li, Q.G. Zhai, Competitive coordination-oriented monodispersed ruthenium sites in conductive MOF/LDH hetero-nanotree catalysts for efficient overall water splitting in alkaline media, *Adv. Mater.* 34 (12) (2022) e2107488.
- [15] P. Zhai, M. Xia, Y. Wu, G. Zhang, J. Gao, B. Zhang, S. Cao, Y. Zhang, Z. Li, Z. Fan, et al., Engineering single-atomic ruthenium catalytic sites on defective nickel-iron layered double hydroxide for overall water splitting, *Nat. Commun.* 12 (1) (2021) 4587.
- [16] X. Zou, A. Goswami, T. Asefa, Efficient noble metal-free electro catalysis of water and alcohol oxidations by zinc-cobalt layered double hydroxide, *J. Am. Chem. Soc.* 135 (46) (2013) 17242.
- [17] C. Xie, Y. Wang, K. Hu, L. Tao, X. Huang, J. Huo, S. Wang, In situ confined synthesis of molybdenum oxide decorated nickel-iron alloy nanosheets from MoO₄²⁻ intercalated layered double hydroxides for the oxygen evolution reaction, *J. Mater. Chem. A* 5 (1) (2017) 87.
- [18] R. Liu, Y. Wang, D. Liu, Y. Zou, S. Wang, Water-plasma-enabled exfoliation of ultrathin layered double hydroxide nanosheets with multivacancies for water oxidation, *Adv. Mater.* 29 (30) (2017) 1701546.
- [19] B.M. Hunter, W. Hieringer, J.R. Winkler, H.B. Gray, A.M. Müller, Effect of interlayer anions on NiFe-LDH nanosheet water oxidation activity, *Energy Environ. Sci.* 9 (5) (2016) 1734.
- [20] J. Liu, H. Wang, L. Wang, P. Jian, X. Yan, Phase-dependent catalytic performance of MnO₂ for solvent-free oxidation of ethylbenzene with molecular oxygen, *Appl. Catal. B: Environ.* 305 (2022) 121050.
- [21] X. Jia, Y. Zhao, G. Chen, L. Shang, R. Shi, X. Kang, G.I.N. Waterhouse, L.-Z. Wu, C.-H. Tung, T. Zhang, Ni₃FeN Nanoparticles derived from ultrathin NiFe-layered double hydroxide nanosheets: an efficient overall water splitting electrocatalyst, *Adv. Energy Mater.* 6 (10) (2016) 1502585.
- [22] Y. Yang, J. Zhou, F. Zhu, Y. Yuan, D.J. Chang, D.S. Kim, M. Pham, A. Rana, X. Tian, Y. Yao, et al., Determining the three-dimensional atomic structure of an amorphous solid, *Nature* 592 (7852) (2021) 60.
- [23] S. Hong, C.S. Lee, M.H. Lee, Y. Lee, K.Y. Ma, G. Kim, S.I. Yoon, K. Ihm, K.J. Kim, T. J. Shin, et al., Ultralow-dielectric-constant amorphous boron nitride, *Nature* 582 (7813) (2020) 511.
- [24] B. Wang, G.M. Biesold, M. Zhang, Z. Lin, Amorphous inorganic semiconductors for the development of solar cell, photoelectrocatalytic and photocatalytic applications, *Chem. Soc. Rev.* 50 (12) (2021) 6914.
- [25] J. Lv, L. Wang, R. Li, K. Zhang, D. Zhao, Y. Li, X. Li, X. Huang, G. Wang, Constructing a Hetero-interface Composed of Oxygen Vacancy-Enriched Co₃O₄ and crystalline-amorphous NiFe-LDH for oxygen evolution reaction, *ACS Catal.* 11 (23) (2021) 14338.
- [26] J. Liu, H. Tang, P. Jian, B. Liu, Oxygen-vacancy defect engineering to boost the aerobic oxidation of limonene over Co₃O₄ nanocubes, *Appl. Catal. B: Environ.* 334 (2023) 122828.
- [27] Y. He, L. Liu, C. Zhu, S. Guo, P. Golani, B. Koo, P. Tang, Z. Zhao, M. Xu, C. Zhu, et al., Amorphizing noble metal chalcogenide catalysts at the single-layer limit towards hydrogen production, *Nat. Catal.* 5 (3) (2022) 212.
- [28] H. Han, H. Choi, S. Mhin, Y.-R. Hong, K.M. Kim, J. Kwon, G. Ali, K.Y. Chung, M. Je, H.N. Umh, et al., Advantageous crystalline-amorphous phase boundary for enhanced electrochemical water oxidation, *Energy Environ. Sci.* 12 (8) (2019) 2443.
- [29] Y. Hu, G. Luo, L. Wang, X. Liu, Y. Qu, Y. Zhou, F. Zhou, Z. Li, Y. Li, T. Yao, et al., Single Ru atoms stabilized by hybrid amorphous/crystalline FeCoNi layered double hydroxide for ultraefficient oxygen evolution, *Adv. Energy Mater.* 11 (1) (2020) 2002816.
- [30] M.F. Lichterman, A.I. Carim, M.T. McDowell, S. Hu, H.B. Gray, B.S. Brunschwig, N. S. Lewis, Stabilization of n-cadmium telluride photoanodes for water oxidation to O₂(g) in aqueous alkaline electrolytes using amorphous TiO₂ films formed by atomic-layer deposition, *Energy Environ. Sci.* 7 (10) (2014) 3334.
- [31] Y. Jiao, R. Sharpe, T. Lim, J.W.H. Niemantsverdriet, J. Gracia, Photosystem II acts as a spin-controlled electron gate during oxygen formation and evolution, *J. Am. Chem. Soc.* 139 (46) (2017) 16604.
- [32] S. Zhang, Y. Zhao, R. Shi, C. Zhou, G.I.N. Waterhouse, L.Z. Wu, C.H. Tung, T. Zhang, Efficient photocatalytic nitrogen fixation over Cu²⁺-modified defective ZnAl-layered double hydroxide nanosheets, *Adv. Energy Mater.* 10 (8) (2020) 1901973.
- [33] T.H. Tan, B. Xie, Y.H. Ng, S.F.B. Abdullah, H.Y.M. Tang, N. Bedford, R.A. Taylor, K.-F. Aguey-Zinsou, R. Amal, J. Scott, Unlocking the potential of the formate pathway in the photo-assisted Sabatier reaction, *Nat. Catal.* 3 (12) (2020) 1034.
- [34] R. Schaub, P. Thosttrup, N. Lopez, E. Laegsgaard, I. Stensgaard, J.K. Norskov, F. Besenbacher, Oxygen vacancies as active sites for water dissociation on rutile TiO₂(2)(110), *Phys. Rev. Lett.* 87 (26) (2001) 266104.
- [35] Y. Li, Z. Liu, Z. Rao, F. Yu, W. Bao, Y. Tang, H. Zhao, J. Zhang, Z. Wang, J. Li, et al., Experimental and theoretical insights into an enhanced CO₂ methanation mechanism over a Ru-based catalyst, *Appl. Catal. B: Environ.* 319 (2022) 121903.
- [36] Z.F. Huang, J. Song, Y. Du, S. Xi, S. Dou, J.M.V. Nsanizimana, C. Wang, Z.-J. Xu, X. Wang, Chemical and structural origin of lattice oxygen oxidation in Co-Zn oxyhydroxide oxygen evolution electrocatalysts, *Nat. Energy* 4 (4) (2019) 329.

- [37] L. Zhuang, L. Ge, Y. Yang, M. Li, Y. Jia, X. Yao, Z. Zhu, Ultrathin iron-cobalt oxide nanosheets with abundant oxygen vacancies for the oxygen evolution reaction, *Adv. Mater.* 29 (17) (2017) 1606793.
- [38] Y. Fang, Y. Xue, L. Hui, H. Yu, Y. Li, Graphdiyne@Janus magnetite for photocatalytic nitrogen fixation, *Angew. Chem. Int. Ed.* 60 (6) (2021) 3170.
- [39] X. Han, L. Gu, Z. Sun, M. Chen, Y. Zhang, L. Luo, M. Xu, S. Chen, H. Liu, J. Wan, et al., Manipulating charge-transfer kinetics and a flow-domain LiF-rich interphase to enable high-performance micro-sized silicon-silver-carbon composite anodes for solid-state batteries, *Energy Environ. Sci.* 16 (11) (2023) 5395.
- [40] W.A. Saoud, A.A. Assadi, M. Guiza, S. Loganathan, A. Bouzaza, W. Aboussaoud, A. Ouederni, S. Rtimi, D. Wolbert, Synergism between non-thermal plasma and photocatalysis: implications in the post discharge of ozone at a pilot scale in a catalytic fixed-bed reactor, *Appl. Catal. B: Environ.* 241 (2019) 227.
- [41] J.E. Perez-Aguilar, C.Y. Chen, J.T. Hughes, C.Y. Fang, B.C. Gates, Isostructural atomically dispersed rhodium catalysts supported on SAPO-37 and on HY Zeolite, *J. Am. Chem. Soc.* 142 (26) (2020) 11474.
- [42] J. Wang, Z. Wu, Q. Niu, L. Liu, L. Yang, M. Fu, D. Ye, P. Chen, Highly efficient adsorptive removal of toluene using silicon-modified activated carbon with improved fire resistance, *J. Hazard. Mater.* 415 (2021) 125753.